Journal of The Electrochemical Society, 2024 171 100512 1945-7111/2024/171(10)/100512/5/\$40.00 © 2024 The Electrochemical Society ("ECS"). Published on behalf of ECS by IOP Publishing Limited. All rights, including for text and data mining, AI training, and similar technologies, are reserved.





Visualizing and Quantifying Electronic Accessibility in Composite **Battery Electrodes using Electrochemical Fluorescent Microscopy**

Karla Negrete¹ and Maureen H. Tang^{1,2,*,z}

 I Department of Mechanical Engineering and Mechanics, Drexel University, Philadelphia, Pennsylvania 19104, United States of America

Electronic connections between active material particles and the conductive carbon binder domain govern high-energy commercial Li-ion batteries' rate capability and lifetime (LIB). This work develops an in situ electrochemical fluorescent microscopy (EFM) technique that maps fluorescence intensity to these local electronic connections. Specifically, rapid redox kinetics of an electrofluorophore translates to reaction distributions limited by the electronic accessibility of battery electrode regions and individual active material particles. This technique can visualize hot spots, dead zones, and isolated particles on the electrode surface. EFM characterization of a series of LiNi_{0.33}Mn_{0.33}Co_{0.33}O₂ electrodes across processing parameters finds a significant negative correlation between the number of disconnected active particles and the rate capability. This low-cost technique provides quantitative mesoscale characterization of commercial LIB electrodes with fast throughput (<60 s) to facilitate rapid research and development and provide manufacturing quality control.

© 2024 The Electrochemical Society ("ECS"). Published on behalf of ECS by IOP Publishing Limited. All rights, including for text and data mining, AI training, and similar technologies, are reserved. [DOI: 10.1149/1945-7111/ad81b6]

Manuscript submitted August 9, 2024; revised manuscript received September 19, 2024. Published October 10, 2024.

Supplementary material for this article is available online

Exploiting high-energy materials in commercial lithium-ion batteries requires fully utilizing these active materials while minimizing inactive components such as the conductive carbon binder domain (CBD). Electronic resistance between active material particles and the CBD is known to prevent full state-of-charge (SOC) in battery operations. ^{1,2}Many studies have shown that, at commercially relevant concentrations of active material (> 95 wt%), performance is limited by short-range electronic contacts between particles of cathode active material and the CBD, rather than ion transport. 1,3-6 Furthermore, electrode failure over long cycling typically occurs at isolated or weakly connected particles that experience extreme voltages.^{6,7} Direct measurement of local, particle-scale electronic contacts would therefore enable rapid prediction of electrode performance for improved battery research and manufacturing quality control.

Despite the importance of these contacts, no existing method can measure them directly. Electrochemical impedance spectroscopy (EIS) cannot characterize particle-to-particle resistances, since measurements reflect the path of least resistance. Measurements of electronic resistances at the sub-mm scale have been conducted using a fourpoint probe with dimensions of 70–200 um. 9,10 Limitations of probe spacing, as well as the line-scan nature of this technique, make it unsuitable for characterizing single-particle contacts. In an alternative approach, the reflectivity of active metal oxide particles has been linked to state-of-charge using operando spectroscopic or combinatorial microscopic techniques, such as operando optical microscopy and modeling, 11 scattering, 12 or reflectance microscopy. 13 Yet, these microscopy methods risk skewed results stemming from differences in reflectivity at particle interfaces, leading to artifacts between particles that may mimic heterogeneities. ¹⁴ This is particularly relevant for composite battery electrodes, where thicknesses and roughness can vary widely. 15 Beyond this, many of these techniques are available only at specialized synchrotron facilities, which are unavailable to most researchers. A high-throughput technique based on easily accessible equipment would permit researchers throughout academia and industry to elucidate the relationship between electronic accessibility and battery performance.¹⁵

We hypothesized that in situ electrochemical fluorescent microscopy (EFM) could visualize and quantify local electronic contacts between active material particles and the CBD in commercial LIB

*Electrochemical Society Member.

^zE-mail: mhtang@drexel.edu

composite electrodes. Fluorescent microscopy offers fast (<100 ms), high-resolution (800 nm)¹⁶ imaging capabilities over large areas, enabling in-depth spatial and temporal analysis. ^{17,18} Our technique relies on the principle of electrofluorochromism, in which fluorescence is reversibly (de)activated upon electrochemical redox. Previously, EFM has been used to measure spatial state-of-charge in an operando flow battery¹⁸ but has not been used to characterize traditional Li-ion composite electrodes. Here, particles of LiNi_{0,33}Mn_{0,33}Co_{0,33}O₂ (NMC111) that are well connected to the current collector via the conductive CBD can transfer an electron to the fluorophore, while particles or regions with high electronic resistance are not reactive (Fig. 1). The fluorescent intensity therefore corresponds to the local reaction rate, which is in turn limited by electronic connectivity.

Methodology

Materials.—9,10 Anthraquinone (AQ, 98%), tetraethylammonium tetrafluoroborate (TEBAF₄, 99%), and anhydrous propylene carbonate (PC, 99.7%) were purchased from Millipore Sigma. AQ was stored in an argon-filled glovebox (O2 < 21.7 PPM, H2O < 1.2 PPM). TEABF4 was dried at overnight 120 C under 0.9 Mpa in a vacuum oven before being transferred to the glovebox. Solutions of 0.1 M TEABF4 in PC were further dried with 3 A molecular sieves (Millipore Sigma) for 72 h. PC was selected for this application for its strong anion solvation, resistance to dimerization, and similarity to battery solvents. Solutions were stored in amber vials to minimize light-induced side reactions or quenching.

Electrochemical characterization.—Electrochemical characterization of AO was conducted with a BioLogic potentiostat in a glovebox with a 3 mm glassy carbon disk working electrode (Basi), platinum wire counter electrode, and platinum wire pseudo-reference electrode. The platinum pseudo-reference electrode was calibrated as $-0.79 \,\mathrm{V}$ vs the ferrocene/ferrocenium redox couple, which has a known potential of 3.25 V vs Li/Li⁺.

Fluorescence spectroscopy.—Fluorometry was conducted using a Shimadzu Spectro-fluorophotometer RF-6000 on neutral and electrolyzed AQ solutions. The neutral solution consisted of 10 mM AQ in 0.1 M TEABF₄ in PC. The solution was electrolyzed for 8 minutes in a three-electrode cell at $-0.56\,\mathrm{V}$ vs reference (1.95 V vs Li/Li⁺) corresponding to the expected potential of the first reduction reaction. Solutions were tested immediately after electrolysis to prevent oxidation or photoreduction.

²Department of Chemical and Biological Engineering, Drexel University, Philadelphia, Pennsylvania 19104, United States of America

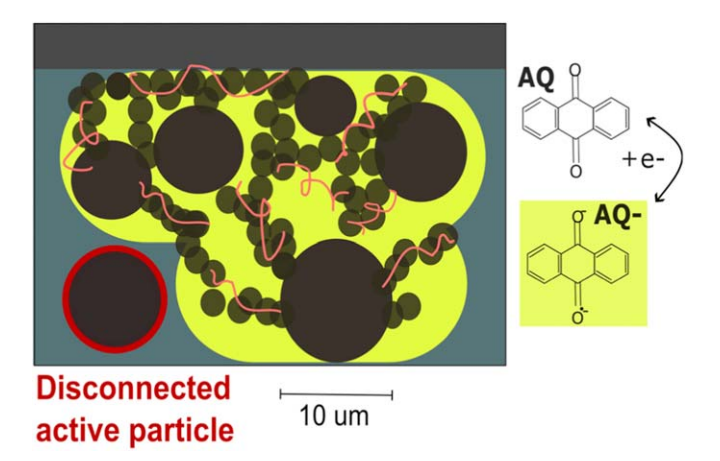


Figure 1. Schematic cross-section of the EFM principle. Well-connected NMC particles in the CBD network transfer electrons to reduce the fluorophore, resulting in uniform fluorescence. Disconnected particles do not fluoresce

Battery testing.—NMC111 electrode sheets were obtained from a previous study 3,4 and vacuum-dried overnight at 120 °C to eliminate residual moisture. These electrodes contained 95 wt% of LiNi(0.33)Mn(0.33)Co(0.33)O2 (NMC) with 10 μm average particle size, 2.5 wt% carbon black, 2.5 wt% PVDF, and diverse processing parameters. The rate capability of these in-house NMC111 electrodes was previously reported by averaging across four-coin cells. In-house NMC111 electrodes were compared to a purchased NMC532 electrode from MTI, used without modification. Purchased NMC532 electrodes underwent electrochemical testing with an Arbin battery cycler. Five-coin cells were conditioned over four cycles at 0.1 C from 3.0 to 4.3 V, then discharged at rates of 0.5, 1, 2, 5, 10, and again at 0.5 C. Cells were charged at 0.1 C between discharges.

In-situ optical experiments.—10 mm electrode discs were punched and arranged in an ECC-Opto-10 optical cell (El-cell) with a face-to-face orientation. The cell included a composite or foil working electrode, a 25 µm-thick PTFE separator with laser-cut holes (McMaster), and a custom 1.1 mm thick conductive FTO window (Saida Glass Co.), all assembled and sealed inside the glovebox. Electrolyte concentration is kept constant at 10 mM AQ in 0.1 M TEABF4 in propylene carbonate, so its influence between samples is minimal. A concentration of 10 mM AQ offered the best performance, balancing between anion dimerization and irreversible electrochemistry at higher concentrations with low fluorescent signals at lower concentrations. Images were acquired using a Zeiss AxioObserver wide-field microscope equipped with 375 nm excitation and 515 nm emission filters, utilizing Objective EC Plan-Neofluar 5x/0.16 M27 (low magnification) and Objective LD Plan-Neofluar 20x/0.4 Corr Ph2 M27 (high magnification) lenses, while applying constant current with a BioLogic potentiostat.

Results and Discussion

We selected the fluorophore 9,10-anthraquinone (AQ) which in its neutral state is non-fluorescent, but upon electrochemical reduction fluoresces at 475 nm when excited at 375 nm.²⁰ We select AQ primarily due to its electrochemical reversibility, fast kinetics, and reduction potential which is well outside the operating potential regions for LIB cathode materials. AQ is reduced to fluorescent AQ⁻ at 1.95 V vs Li/Li⁺ before a second reduction to non-fluorescent AQ²⁻ at 1.40 V vs Li/Li⁺ (Fig. 2C).²¹ The scan-rate dependence of AQ (Fig. S1) shows minimal peak splitting, indicating reversible kinetics. These results confirm that the first reduction reaction will be limited by the electronic accessibility of the electrode, not the intrinsic reaction kinetics. Fluorometry of 1 mM AQ, before and

after electrolysis at 1.95 V vs Li/Li⁺ in Fig. 2D confirms that the radical anion is excited at 375 nm and emits at 475 nm, with a stoke shift of 95 nm.²² A Stokes shift greater than 70 nm provides better resolution during microscopy.²³ The fluorescent signal increases by 200% after electrolysis, confirming that electrochemical reduction of AO at 1.95 V produces the fluorescent radical anion.¹⁸

To demonstrate the direct manipulation of fluorescence via electrochemical reduction, we conducted in situ chronopotentiometry. Stringent sealing against atmospheric oxygen was accomplished in a commercial optical cell (El-cell), which is compatible with a widefield microscope. The electrochemical cell houses a 10 mm composite battery electrode as the working electrode (WE). A custom transparent conductor (fluorine-doped tin oxide, FTO) window as the counter electrode (CE) allows visualization of the electrode surface while electrochemically regenerating the reduced fluorophore (Fig. 2A). An ultra-thin (25.4 um) non-porous polytetrafluoroethylene (PTFE) separator is positioned between the conductive window CE and WE. Precision laser-cut holes constrain the reaction to 1 mm diameter regions of interest (ROIs); this geometry facilitates straightforward visualization and rapid fluorophore diffusion due to the absence of porosity and tortuosity.

In-situ EFM of a commercial NMC electrode is shown in Fig. 3A. We monitored fluorescence while incrementally increasing the reduction current density from the open circuit to -2.5, -5.1, and -7.6 mA cm⁻². Cell voltages recorded during EFM reflect a two-electrode measurement. Although the system does not (de) intercalate Li+, these current densities correspond to C-rates of approximately 2 C, 3 C, and 4 C. In the absence of current (t = 0), no fluorescence was observed. As current increased, fluorescence also increased, consistent with expectations. Upon stopping the current flow at 180 s, fluorescence decayed rapidly as AQ diffused away from the surface. Figure 3 demonstrates a clear mechanism for modulating fluorescence via cathodic current. The diffusion-limited current for AQ, based on Fick's Law, is calculated as -9.23 mA cm⁻² (approximately 6 C). Consistent with theory, we found that exceeding this current led to electrolyte decomposition, gas bubbles, and the formation of the AQ²⁻ dianion. Limiting current densities to 80% of this limiting current optimizes the tradeoff between higher fluorescent signal and experimental complications. In all subsequent EFM experiments, the cathodic current was limited to $-7.6 \,\mathrm{mA} \,\mathrm{cm}^{-2}$ for under 60 seconds to eliminate fluorescent interference between ROI measurements.

Having established the relationship between applied current, AQ formation, and fluorescent intensity, we next determine how fluorescent images relate to electronic accessibility. Commercial electrodes (95% NMC532, 2.5% carbon, 2.5% PVDF) have been highly optimized and should yield highly uniform electronic connectivity with low resistances between individual particles and the CBD despite the high loading of active material. In contrast, electrodes fabricated in-house (95% NMC111, 2.5% carbon, 2.5% PVDF) have highly variable performance depending on processing conditions.^{3,4} These are denoted as "high performance" and "low performance" electrodes, respectively. Although the metal oxide stoichiometry differs, NMC111 and NMC532 are both electronic insulators and should therefore behave identically for EFM. Moreover, during EFM the only reaction expected is an outer sphere electron transfer reaction of the fluorophore, which occurs at voltage ranges well outside the operating potentials of NMC. Thus, surface composition is unlikely to affect EFM images. Figure 4 shows EFM images of both electrodes. At a low-numerical-aperture (NA) microscope objective, with a minimum lateral resolution of 1.51 μm, the entire 1 mm ROI is relatively homogeneous for the highperformance electrode, while the low-performance electrodes show dark spots, both in isolation and agglomerations. A higher-NA object, with a minimum lateral resolution of 0.61 µm, reveals that the low-performance electrode exhibits dark blobs of approximately 10 µm in diameter. We attribute these blobs to isolated particles of NMC based on the excellent match between particle size, shape, and diameter as well as consistency with our hypothesized mechanism

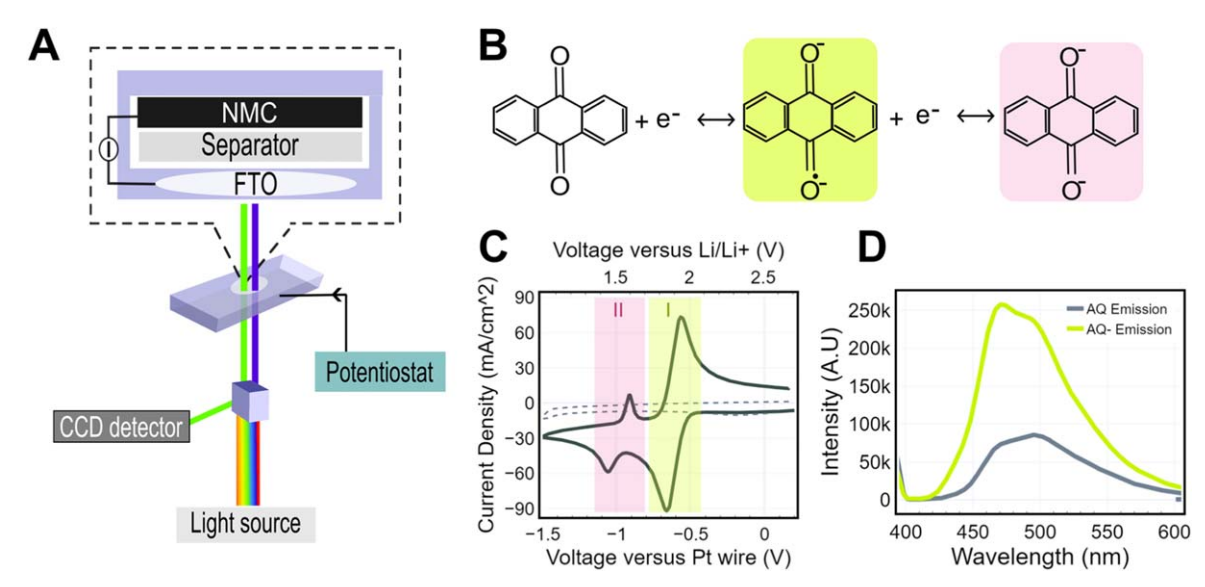


Figure 2. In-situ electrochemical fluorescent microscopy platform. (A) Schematic of electrochemical cell and imaging apparatus (B) 1e- and 2e- reductions for 9,10 anthraquinone (AQ) (C) Voltammogram of fluorophore system showing successive reductions of AQ in 0.1 M TEABF₄: PC at 100 mV s⁻¹. Ferrocene calibration converts from a Pt-pseudo to a Li/Li+ reference system. A background scan of 0.1 M TEABF₄: PC represented by the dotted line. (D) Emission spectra of neutral AQ and radical AQ-.

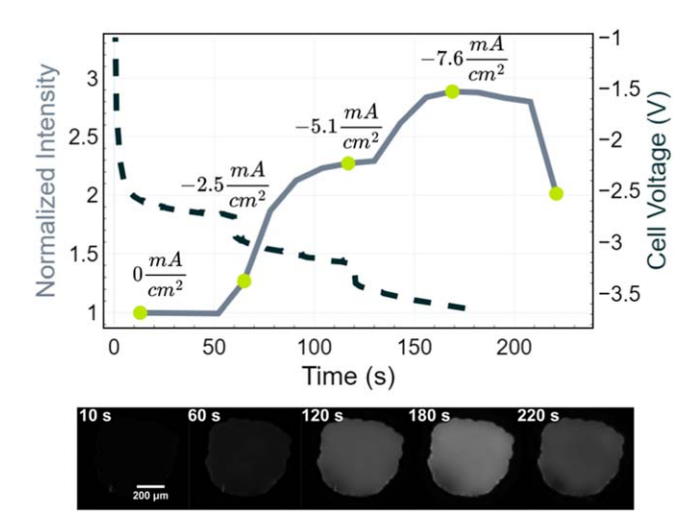


Figure 3. Evolution of in situ fluorescence of NMC electrode. Lower magnification objective (5x/0.16) tracking fluorescence of 1 mm ROI over time with incremental reductive currents. Cell voltage reflects a two-electrode measurement. Rapid fluorescence decay is observed at $t=220\,\mathrm{s}$ post-current flow due to diffusion of AQ^- away from the ROI.

(Fig. 4D). High-performance electrodes, in contrast, exhibit a more uniform fluorescence with fewer dark blobs (Fig. 4B). SEM images reveal that the average observed diameter of purchased NMC532 is 6.33 μ m, whereas the average of the in-house NMC111 is 12.2 μ m (Figs. S5B, S5F). The distinct patterning observed during EFM of NMC532's active particles may be due to differences in surface topology, evident in SEM images as well as the electronic accessibility of particles. Surface topology contributes to the heterogeneity that EFM aims to detect. Overall, when compared to poorly processed electrodes (Fig. 4D), purchased NMC is still objectively more uniform in fluorescence and has many fewer discrete dark blobs.

Figure 4 shows qualitatively that dark blobs corresponding to electronically isolated particles are more prevalent in low- than in high-performance electrodes. To quantitatively correlate the number of dark blobs to battery rate performance, we performed EFM on a library of low- and high-performing NMC electrodes, as measured by coin-cell rate capability data. ^{3,4} We capture high magnification

EFM images in under 60 s while passing a current of -7.6 mA cm⁻². Subsequently, image processing and analysis were conducted on a substantial and swiftly acquired image dataset (N = 103), which was refined to exclude samples that suffered from visible scratches or cracking, gas bubble formation, or extraneous debris (N = 78). Figure S6 shows examples of these artifacts, which prevented focus and rendered images unsuitable for analysis using our algorithm. We then apply a physics-informed segmentation method to classify dark blobs as isolated particles or optical artifacts (Fig. 4E). Image intensities are first normalized from 0 to 1, then binarized using the 65th percentile of the median intensity as a method to dynamically delineate the darkest pixels for segmentation. Domain-specific knowledge of particle Feret diameter and circularity guides the filtering of segmented regions. For instance, only blobs with a diameter consistent with the known diameter (5-7 µm for NMC532, Fig. S5B, and 7-12 μm for NMC111, Fig. S5F) are included in the analysis. Therefore, segmented particles outside these specified diameter ranges were excluded from the count (Fig. 4F). Similarly, only blobs with circularity values from 0.7 to 1 were counted (Fig. 4G). Correlating the average number of segmented particles per electrode ROI with the electrode discharge capacity at 1 C reveals a statistically significant negative relationship (regression coefficient: -0.169, 97.5% CI, p = 0.0237). A Pearson correlation coefficient (PCC) measures the linear relationship between the two variables; we determine a value of -0.736, indicating a strong negative linear correlation. The markers in Fig. 4I reflect the average number of detected blobs per electrode image, with the largest marker size representing a sample set of 14 images and the smallest corresponding to 5 images. We highlight that purchased NMC532 consistently exhibits a low frequency of detected blobs; however, we suspect this is an overestimation, with patterned speckling contributing to false positives due to imperfect segmentation of speckles larger than average or lower intensity. While our blob delineation algorithm is straightforward, it still suffers from imprecise seeding of regions for segmentation. To ensure that only particle-like blobs are included in our analysis excluding shadows and artifacts—robust filtering becomes significant, even if it means discounting true positives within agglomerates.

Conclusions

In summary, we have introduced a low-cost, accessible method to rapidly study electronic resistances in composite electrodes. EFM

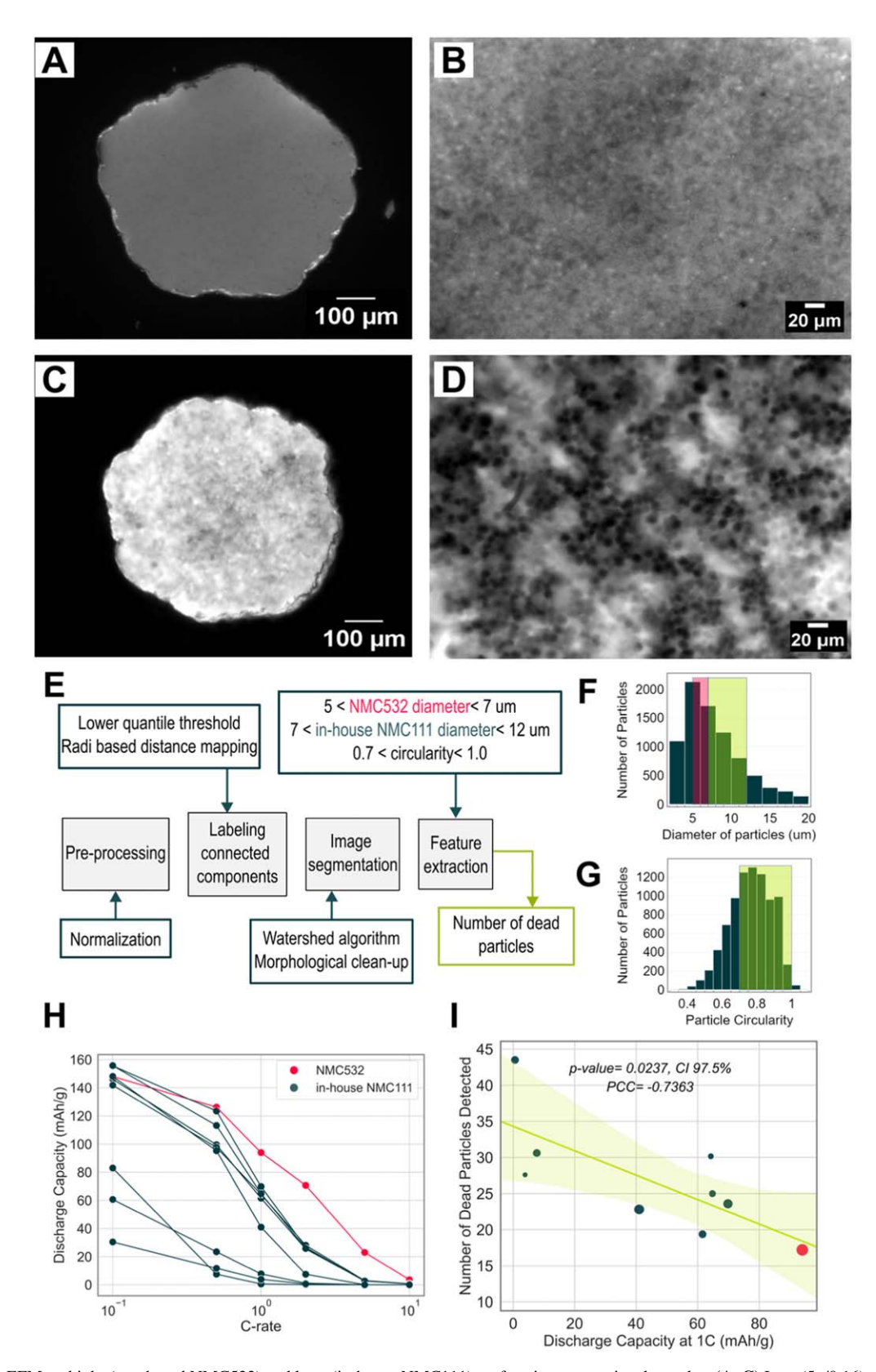


Figure 4. In-situ EFM on high- (purchased NMC532) and low- (in-house NMC111) performing composite electrodes. (**A, C**) Low (5x/0.16) magnification EFM of 1 mm ROI on high- and low- performing electrodes, respectively. (**B, D**) High (20x/0.4) magnification EFM images of high- and low-performing electrodes, revealing particle-to-particle resolution. (**E**) Particle delineation workflow. (**F**) Particle size distribution of segmented particles. The diameter filter is highlighted in green for in-house NMC111 and in red for purchased NMC532. (**G**) Circularity distribution of segmented particles, filter highlighted in green. (**H**) Rate capability results from high- and low- performance electrodes. (I) Relationship between the number of segmented, filtered dead particles and discharge capacity at 1 C, normalized by number of images. Blue lines and markers correspond to NMC111 electrodes, and red corresponds to NMC532.

enables the differentiation of distinct features linked to variations in electronic connectivity among particles within electrodes. We offer a straightforward example of feature extraction to illustrate this method's potential for relating images of electronic connectivity to battery performance. EFM is material-agnostic and can be used to characterize many composite electrodes with micron-scale particle sizes (Fig. S8). We suggest that the relative speed and ease of this experimental method may find utility as a tool for quality control in manufacturing or a rapid prediction method in research and development.

Acknowledgments

This work was supported by the National Science Foundation CBET-1751553. We acknowledge Dr. Andrew Wong of Lawrence Livermore National Laboratory, Dr. Harini Sreenivasappa, and Prof. Aaron Fafarman of Drexel University for their helpful discussions. We also would like to acknowledge Renee M. Saraka of Arkema for the in-house electrode samples and Rayan Alaufey of Drexel University for helping acquire SEM micrographs.

ORCID

Maureen H. Tang https://orcid.org/0000-0003-0037-4814

References

- Y. Li et al., "Effects of particle size, electronic connectivity, and incoherent nanoscale domains on the sequence of lithiation in LiFePO₄ porous electrodes." Adv. Mater., 27, 6591 (2015).
- M. Ebner, F. Marone, M. Stampanoni, and V. Wood, "Visualization and quantification of electrochemical and mechanical degradation in Li Ion batteries." *Science*, 342, 716 (2013).
- S. L. Morelly, N. J. Alvarez, and M. H. Tang, "Short-range contacts govern the performance of industry-relevant battery cathodes." *J. Power Sources*, 387, 49 (2018).
- R. M. Saraka, S. L. Morelly, M. H. Tang, and N. J. Alvarez, "Correlating processing conditions to short- and long-range order in coating and drying lithiumion batteries." ACS Appl. Energy Mater., 3, 11681 (2020).
- P. Albertus, J. Christensen, and J. Newman, "Experiments on and modeling of positive electrodes with multiple active materials for lithium-ion batteries." *J. Electrochem. Soc.*, 156, A606 (2009).
- Y. Li et al., "Current-induced transition from particle-by-particle to concurrent intercalation in phase-separating battery electrodes." *Nature Mater.*, 13, 1149 (2014).

- A. J. Merryweather, Q. Jacquet, S. P. Emge, C. Schnedermann, A. Rao, and C. P. Grey, "Operando monitoring of single-particle kinetic state-of-charge heterogeneities and cracking in high-rate li-ion Anodes." *Nat. Mater.*, 21, 1306 (2022).
- P. Vadhva, J. Hu, M. J. Johnson, R. Stocker, M. Braglia, D. J.-L. Brett, and A. J.-E. Rettie, "Electrochemical impedance spectroscopy for all-solid-state batteries: theory, methods and future outlook." *Chem. Electro. Chem.*, 8, 1930 (2021).
- B. J. Lanterman, A. A. Riet, N. S. Gates, J. D. Flygare, A. D. Cutler, J. E. Vogel, D. R. Wheeler, and B. A. Mazzeo, "Micro-four-line probe to measure electronic conductivity and contact resistance of thin-film battery electrodes." *J. Electrochem.* Soc., 162, A2145 (2015).
- S. W. Peterson and D. R. Wheeler, "Direct measurements of effective electronic transport in porous li-ion electrodes." *J. Electrochem. Soc.*, 161, A2175 (2014).
- X. Lu et al., "Multiscale dynamics of charging and plating in graphite electrodes coupling operando microscopy and phase-field modelling." *Nat. Commun.*, 14, 5127 (2023).
- R. Pandya et al., "Three-dimensional operando optical imaging of particle and electrolyte heterogeneities inside li-ion batteries." *Nat. Nanotechnol.*, 18, 1185 (2023)
- A. J. Merryweather, C. Schnedermann, Q. Jacquet, C. P. Grey, and A. Rao, "Operando optical tracking of single-particle ion dynamics in batteries." *Nature*, 594 522 (2021)
- S. D. Kang and W. C. Chueh, "Probing the depths of battery heterogeneity." Nat. Nanotechnol., 18, 1130 (2023).
- J. Ortega Arroyo, D. Cole, and P. Kukura, "Interferometric scattering microscopy and its combination with single-molecule fluorescence imaging." *Nat. Protoc.*, 11, 617 (2016).
- M.-M. Chen, C.-H. Xu, W. Zhao, H.-Y. Chen, and J.-J. Xu, "Super-resolution electrogenerated chemiluminescence microscopy for single-nanocatalyst imaging." *J. Am. Chem. Soc.*, 143, 18511 (2021).
- N. A. Padilla et al., "Tracking lithium ions via widefield fluorescence microscopy for battery diagnostics." ACS Sens., 2, 903 (2017).
- A. A. Wong, S. M. Rubinstein, and M. J. Aziz, "Direct visualization of electrochemical reactions and heterogeneous transport within porous electrodes in operando by fluorescence microscopy." *Cell Reports Physical Science*, 2, 100388 (2021).
- C. O. Laoire, E. Plichta, M. Hendrickson, S. Mukerjee, and K. M. Abraham, "Electrochemical studies of ferrocene in a lithium ion conducting organic carbonate electrolyte." *Electrochim. Acta*, 54, 6560 (2009).
- R. G. Compton, A. C. Fisher, and R. G. Wellington, "A thin-layer electrode cell for fluorescence. measurements on electrogenerated intermediates." *Electroanalysis*, 3, 27 (1001)
- K.-B. Kushkhov, Y.-I. Musaev, A. M. Kharaev, A. B. Zhekamukhov, and V. A. Kvashin, "Anthraquinone electroreduction mechanism in 0.1 M tetrabutylammonium bromide in dimethyl sulfoxide." Russ. J. Electrochem., 40, 203 (2004).
- M. Fernández-Suárez and A. Y. Ting, "Fluorescent probes for super-resolution imaging in living cells." Nat. Rev. Mol. Cell Biol., 9, 929 (2008).
- Z. Gao, Y. Hao, M. Zheng, and Y. Chen, "A fluorescent dye with large stokes shift and high stability: synthesis and application to live cell imaging." RSC Adv., 7, 7604 (2017).